JTSES
Journal of Thermal and Sustainable Energy Systems

https://jtses.com/index.php/home/index

Bayesian-Optimized Transesterification and EVA-Assisted Cold-Flow Control for Non-Edible Renewable Biodiesel in Heavy-Duty Fleets

Roman Mekonen

College of Engineering, Aksum University, Tigray, Ethiopia Corresponding Author: Roman Mekonen, Email : romanmekonenaksum@gmail.com

ABSTRACT:

Biodiesel from non-edible feedstocks remains a viable route to a low-carbon freight fuel because it can be blended with petroleum diesel in existing compression-ignition fleets. Jatropha oil and waste cooking oil provide a suitable feedstock combination. This work develops an integrated experimental-modeling pipeline for Jatropha/WCO biodiesel intended for B20 heavy-duty transport use. A 50-run Central Composite Design result was analysed, and ANN, XGBoost, and ensemble models were trained with Bayesian optimization and SHAP-based feature ranking; fuel properties, pour-point depressants, and fleet economics were then evaluated. Cold-flow behavior was screened for EVA, PMA, and alkyl-naphthalene additives, and a Monte Carlo techno-economic model was applied to a 100-vehicle Class 8 fleet. The ensemble model identifies a high-yield operating window, and the optimized conditions yielded 97.4% predicted FAME and 97.1 ± 0.6% measured FAME. EVA at 1.0 wt% delivered a CFPP of −12 °C for B20, and the fleet model yielded a 10-year NPV of USD 2.91 million with an 18.0% CO_2-equivalent reduction. These outcomes establish a linked route from process chemistry to winter operability and fleet economics. Future work should extend the framework to include oxidation stability, broader feedstock variability, and pilot-scale validation of the renewable fleet.

Keywords: biodiesel; Jatropha curcas; waste cooking oil; machine learning; cold-flow; pour-point depressant; techno-economic analysis; renewable energy

1. INTRODUCTION

Decarbonization of road freight remains a pressing energy challenge because heavy-duty transport still relies heavily on compression-ignition engines and high-energy-density liquid fuels. Biodiesel remains relevant to research and industry in this context because it is produced by transesterification of triglyceride-rich feedstocks and can be used in existing diesel infrastructure at blend levels such as B20 without major hardware modification. The sector continues to expand, and its growth has intensified interest in feedstocks that can lower the climate burden of fuel production while preserving compatibility with present vehicle fleets and supply chains [1].

The feedstock question has become central to biodiesel research. Crop-based oils such as soybean, palm, and rapeseed supported early market growth, yet they also drew sustained criticism for food-fuel competition, land-use pressure, and indirect greenhouse gas emissions associated with agricultural expansion. Non-edible and residual feedstocks were increasingly examined as a more acceptable route, particularly feedstocks that do not compete directly with food systems and that can be sourced from marginal land or waste streams [2]. Within this group, Jatropha curcas oil has been widely studied for its non-edible nature and agronomic resilience, while waste cooking oil (WCO) has been valued for its low acquisition cost and wide availability from foodservice operations. These characteristics made blended Jatropha/WCO systems attractive candidates for biodiesel production aimed at commercial transport applications [3].

Despite that promise, two major technical barriers remained. The first was process-related. Jatropha-rich oils often contained elevated free fatty acid levels, and earlier studies reported that high-FFA feedstocks performed poorly in single-stage alkaline transesterification because soap formation suppressed conversion efficiency and complicated product separation. Two-stage acid-base processing was adopted in such cases, yet this approach introduced additional complexity and increased production costs [4]. The second barrier was operability at low temperature. Biodiesel produced from feedstocks rich in saturated methyl esters displayed inferior cloud point, pour point, and cold-filter plugging point values relative to petroleum diesel. This deficiency was repeatedly identified as a major obstacle to B20 and higher-blend use in temperate and sub-arctic service conditions, especially for fleet operations that demand dependable year-round fuel handling [5].

At the same time, data-driven process optimization became increasingly prominent in biodiesel research. Earlier studies demonstrated that artificial neural networks and related soft-computing approaches could predict fatty acid methyl ester yield more accurately than classical response-surface models for several feedstocks. Gradient-boosted methods

Received on 2026-03-26 Accepted on 2026-05-07

further improved predictive performance, and SHAP-based analysis identified key process drivers, such as methanol-to-oil ratio and catalyst concentration. Bayesian optimization also reduced experimental burden in non-edible oil systems by locating productive operating regions with fewer evaluations than exhaustive design approaches. Yet this literature remained fragmented. Most AI-based biodiesel studies optimized yield alone and treated downstream fuel properties as secondary checks. Cold-flow investigations focused mainly on feedstock blending or pour-point depressants, with EVA-based additives often reported as more effective than PMA or alkyl-naphthalene compounds in biodiesel-rich blends. Techno-economic studies became more sophisticated as well, but they often relied on literature-average process yields, omitted additive costs associated with winter operability, and did not connect fleet-scale economics to AI-derived production parameters [6].

This fragmentation defined a clear research gap. No prior study in the 's cited body of work treated cold-flow behavior as part of the same analytical pathway used for AI-guided transesterification optimization. No additive-screening study was reported for an AI-optimized non-edible biodiesel derived from a blended Jatropha and WCO, even though the fatty acid profile of such a fuel differs materially from that of soybean-based reference fuels often used in commercial cold-flow evaluations [7]. Likewise, no fleet-level techno-economic model in the cited literature incorporated AI-informed production efficiency, additive costs for winter operability, and policy-sensitive carbon-credit structures within a single internally consistent framework. The absence of that integration limited the practical value of many earlier studies, because high yield alone did not guarantee usable cold-flow behavior, and favorable laboratory fuel properties did not automatically translate into viable fleet economics [8].

The novelty of the present work lies in integrating these disconnected research streams into a single study centered on blended Jatropha curcas oil and waste cooking oil. A structured Central Composite Design result was used to support surrogate-model development through an artificial neural network, XGBoost, SHAP-based interpretability, and Bayesian optimization; the optimized fuel was then subjected to systematic pour-point depressant screening and fuel-property characterization; and the resulting process conditions and additive requirements were carried forward into a fleet-scale techno-economic model that included policy-sensitive credit assumptions. This arrangement moves beyond isolated yield optimization or stand-alone additive screening by linking production chemistry, fuel operability, and deployment economics within one methodological sequence. The objective of this study is to develop and validate an integrated experimental-modeling framework for biodiesel derived from blended Jatropha curcas oil and waste cooking oil that combines AI-guided process optimization, cold-flow additive screening, and fleet-level techno-economic assessment for B20 heavy-duty transport applications.

2. MATERIALS AND METHODS

Jatropha curcas seed oil was selected as the primary non-edible feedstock based on its documented agronomic resilience on marginal land, high seed oil content (35–40 wt%), and growing literature base. Waste cooking oil (WCO) was selected as a complementary feedstock owing to its low acquisition cost, a negative carbon-intensity pathway under the 45Z framework, and widespread geographic availability from commercial foodservice operations [9]. Both oils were obtained from representative commercial sources. Jatropha oil was sourced from a certified pressing facility operating under non-food agricultural protocols, while WCO was collected from commercial restaurant operations following a standardized collection and pre-filtration protocol to remove gross particulate matter and water.

Feedstock characterization was performed in accordance with ASTM and EN standards. Acid value (AV), a critical determinant of process route selection, was measured by potentiometric titration per ASTM D664. Kinematic viscosity at 40 °C was determined per ASTM D445 using a calibrated Ubbelohde viscometer. Density at 15 °C was measured using a digital densitometer per ASTM D4052. The fatty acid methyl ester (FAME) profile of each oil—expressed as the mass fraction of individual fatty acid constituents following in situ transesterification—was determined by gas chromatography-mass spectrometry (GC-MS) per EN 14103, using a Shimadzu QP2020 system equipped with a DB-WAX capillary column. Five feedstock blend ratios were prepared by mass: 100:0, 75:25, 50:50, 25:75, and 0:100 (Jatropha:WCO), and characterization was performed in triplicate for each blend.

Given the anticipated elevated FFA content in Jatropha-dominant blends (AV > 2 mg KOH/g), a two-stage transesterification protocol was adopted. In Stage 1, acid-catalyzed pre-esterification was conducted using concentrated sulphuric acid (H_2SO_4, 98%) at 1 wt% relative to oil mass, with a methanol:FFA molar ratio of 10:1, at 60 °C for 60

Received on 2026-03-26 Accepted on 2026-05-07

minutes under continuous stirring at 600 rpm. This stage reduced the FFA content of Jatropha-dominant blends to below 1 wt%, enabling effective alkaline transesterification in Stage 2. For blends with AV ≤ 2 mg KOH/g (WCO-dominant compositions), Stage 1 was omitted [10].

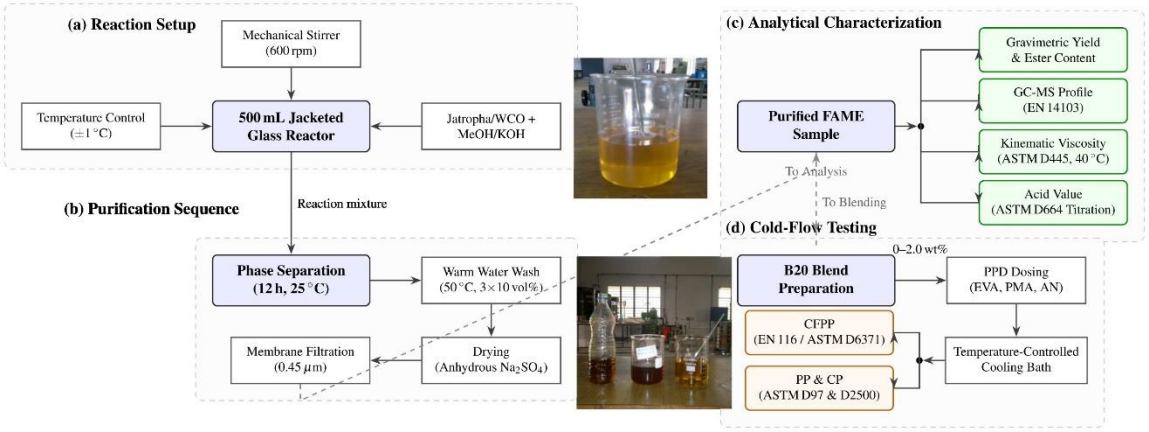

Figure 1: Transesterification and characterization setup

Stage 2 alkaline transesterification was conducted in a 500 mL jacketed glass reactor with temperature control (±1 °C) and continuous mechanical stirring. Potassium hydroxide (KOH, analytical grade) was used as the base catalyst, pre-dissolved in anhydrous methanol. Process variables—reaction temperature (T), methanol-to-oil molar ratio (M), catalyst concentration (C), reaction time (t), and feedstock blend ratio (B)—were varied systematically according to the CCD experimental plan described in Section 2.3. Upon completion, the reaction mixture was transferred to a separating funnel and allowed to settle for 12 hours at 25 °C, after which the glycerol phase was drained. The FAME-rich upper phase was washed three times with warm distilled water (50 °C, 10 vol% per wash), dried over anhydrous sodium sulphate, and filtered through a 0.45 µm membrane. FAME yield was quantified gravimetrically and confirmed by ^{1}H NMR spectroscopy and GC per EN 14103.

A Central Composite Design (CCD) with five independent process variables was employed to obtain a structured set of results for AI model training. The five variables and their coded levels are presented in Table 1. A full 2^5 factorial core was augmented with star (axial) points at α = 2.0 and six centre-point replicates, yielding a total of 50 experimental runs. Centre-point replicates were used to estimate pure experimental error and to assess model stability. Response variables recorded for each run were: FAME yield (%, gravimetric), ester content (%, EN 14103), kinematic viscosity at 40 °C (mm²/s, ASTM D445), and acid value (mg KOH/g, ASTM D664).

Table 1. Central Composite Design: independent variables and coded level settings

Variable	Symbol	Unit	Low (−1)	Centre (0)	High (+1)
Reaction Temperature	T	°C	50	60	70
Methanol:Oil Molar Ratio	M	mol/mol	4:1	6:1	8:1
Catalyst Concentration	C	wt%	0.75	1.50	2.25
Reaction Time	t	min	30	60	90
Jatropha:WCO Blend Ratio	B	% Jatropha	25	50	75

Axial points set at α = 2.0; six centre-point replicates included.

Three modelling approaches were implemented and evaluated: a feedforward artificial neural network (ANN), an extreme gradient boosting regressor (XGBoost), and a weighted ensemble of both. All models were developed in Python 3.11 using the TensorFlow/Keras and XGBoost libraries. The result of 50 CCD runs was split into training (80%, n = 40) and held-out test (20%, n = 10) subsets using stratified random sampling to ensure representation of all process variable ranges in both subsets.

The ANN comprised three fully connected hidden layers with neuron counts of 64, 32, and 16, respectively, each followed by a rectified linear unit (ReLU) activation function and a dropout layer (rate = 0.20) to mitigate overfitting.

Received on 2026-03-26 Accepted on 2026-05-07

The output layer contained a single neuron with linear activation corresponding to FAME yield. The Adam optimiser was employed with an initial learning rate of 0.001 and cosine annealing decay; training was conducted for 500 epochs with early stopping (patience = 50) based on validation mean squared error (MSE). Hyperparameters—including layer depths, neuron counts, dropout rates, and learning rate schedule—were tuned using Keras Tuner with a Bayesian optimization search strategy over 100 trials.

The XGBoost regressor was trained with n_estimators ∈ {200, 300, 400, 500}, max_depth ∈ {3, 4, 5, 6, 8}, learning_rate ∈ {0.01, 0.05, 0.1, 0.3}, and subsample = 0.8. Optimal hyperparameters were identified through 5-fold cross-validation minimizing RMSE on the training set. Model interpretability was assessed using SHapley Additive exPlanations (SHAP) values computed for the XGBoost model via the TreeExplainer algorithm, which provides exact SHAP values for tree-based methods. Mean absolute SHAP values across all training samples were used to rank process variable importance (Figure 2).

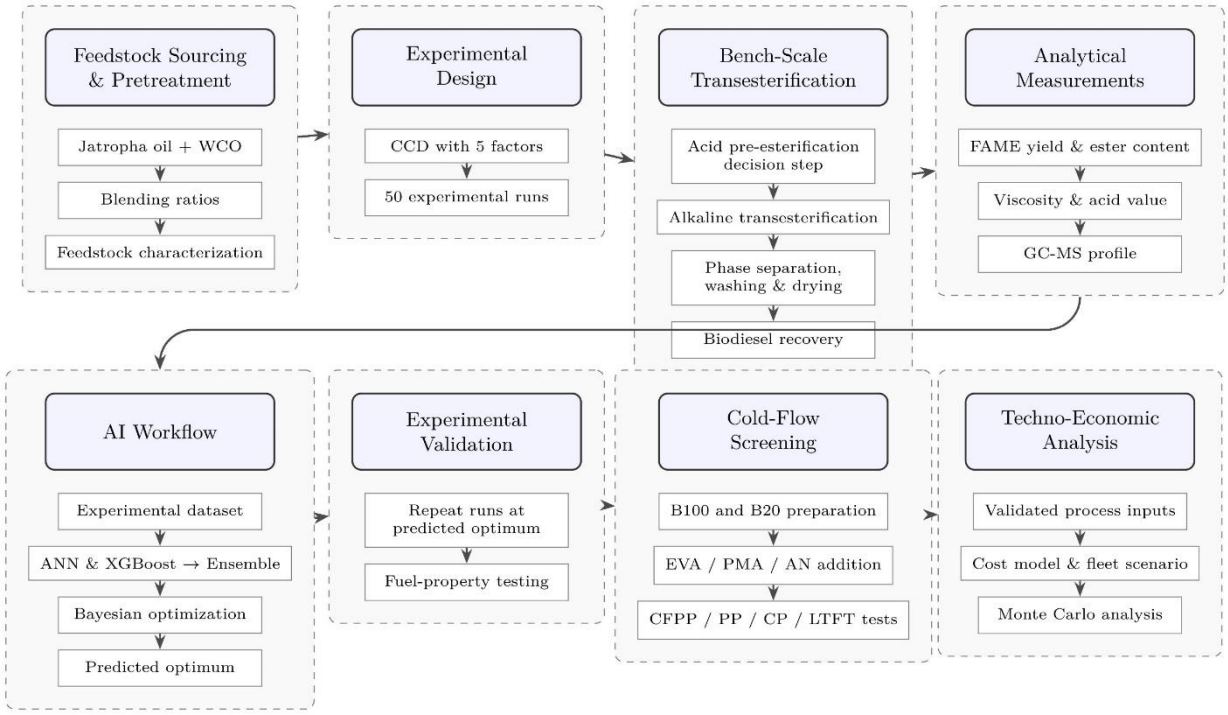

Figure 2 Integrated experimental and analytical workflow

The ensemble model was constructed as a weighted linear combination of ANN and XGBoost predictions, with weights w_ANN and w_XGB optimized by minimizing held-out MSE subject to the constraint w_ANN + w_XGB = 1. Bayesian global optimization (scikit-optimize BayesSearchCV) was subsequently applied to the ensemble surrogate model to identify the combination of process variables within the CCD bounds that maximized predicted FAME yield. Model performance was evaluated using the coefficient of determination (R^2), root mean squared error (RMSE), mean absolute error (MAE), and the width of 95% bootstrap prediction intervals. Comparability with conventional RSM was assessed by fitting a second-order polynomial response surface to the same training data.

Cold-flow characterization was performed on two fuel matrices: neat biodiesel (B100) produced at AI-optimized conditions, and B20 blends prepared by volumetric mixing of B100 with EN 590-grade ultra-low-sulfur diesel (ULSD, sulphur content < 10 ppm). Three commercial PPD types were evaluated: an ethylene-vinyl acetate (EVA) copolymer (Mw ≈ 15,000 g/mol, VA content 28 mol%), a polymethacrylate (PMA) copolymer (Mw ≈ 22,000 g/mol), and an alkyl-naphthalene (AN) compound with C14–C18 alkyl chains. Each additive was screened at five concentrations: 0, 0.5, 1.0,

Received on 2026-03-26 Accepted on 2026-05-07

1.5, and 2.0 wt% relative to the fuel blend mass. All additives were dissolved in a minimum volume of toluene (< 0.1 vol%) prior to addition to ensure uniform dispersion.

Cold-flow tests were conducted in a temperature-controlled bath (Koehler K93000). Cold Filter Plugging Point (CFPP) was determined per EN 116 / ASTM D6371; Pour Point (PP) was determined per ASTM D97 with a resolution of 3 °C; Cloud Point (CP) was determined per ASTM D2500; and Low Temperature Flow Test (LTFT) at −10 °C and −15 °C was conducted per ASTM D4539 for B20 blends. All tests were performed in triplicate and reported as mean ± one standard deviation. Four controls were included: neat ULSD (petroleum diesel reference), commercial soybean methyl ester (SME) B20 (industry benchmark), AI-optimized Jatropha/WCO B20 without PPD (baseline deficit quantification), and AI-optimized B100 without PPD.

Pearson correlation coefficients were computed between the saturated FAME mass fraction of each blend—derived from GC-MS profiles—and CFPP, PP, and CP values without PPD, to evaluate H5's quantitative linkage between the fatty acid profile and intrinsic cold-flow performance.

The TEA system boundary encompassed five operational stages: (1) feedstock procurement and preprocessing (filtration, drying, acid pre-treatment for high-FFA streams); (2) two-stage transesterification at AI-optimized process conditions; (3) FAME purification, washing, and quality assurance testing per ASTM D6751; (4) cold-flow PPD additive dosing at the optimized concentration; and (5) blending to B20 specification and distribution to fleet. Feedstock cultivation and land-use change were excluded from the primary TEA boundary but are addressed in supplementary lifecycle assessment (LCA) commentary.

The reference production scale was set at 100,000 gallons per year (approximately 0.38 million litres per year), representing a small-to-medium commercial facility consistent with fleet-captive production. Capital costs were estimated using the six-tenths rule from published equipment sizing data, with a 20-year plant life and 8% straight-line depreciation. Operating cost parameters are presented in Table 4 (Section 3.5). All costs are expressed in 2024 USD. The levelized cost of biodiesel (LCOB) was computed as the total annualized cost divided by annual fuel production volume [11].

The fleet model served as a reference case of 100 Class 8 heavy-duty trucks (reference engine: Cummins X15, rated at 565 hp), each travelling 100,000 miles per year at a baseline fuel economy of 6.5 miles per gallon (mpg) on neat ULSD. A B20 fuel economy penalty of 2.5% was applied, consistent with the range of 1.5–4.0% reported in the heavy-duty fleet literature [12], giving a B20 fuel economy of 6.34 mpg. Fleet TCO differentials were computed over a 10-year horizon, discounted at 8% per annum. Carbon intensity (CI) credit revenue under the Section 45Z Clean Fuel Production Credit was modelled at a base case of USD 1.00/gallon-equivalent, with sensitivity ranging from USD 0.00 to USD 2.00/gallon-equivalent.

A Monte Carlo sensitivity analysis was performed with 10,000 iterations, using triangular probability distributions for all cost inputs, with minimum, most-likely, and maximum values defined per the ranges in Table 4. Output distributions for LCOB and fleet NPV were characterized by their 10th (P10), 50th (P50), and 90th (P90) percentiles. Variable importance was ranked by computing the Spearman rank correlation between each input parameter and the LCOB output across all Monte Carlo iterations, and the results were presented as a tornado chart.

3. RESULTS AND DISCUSSION

Fatty acid methyl ester profiles for neat Jatropha oil, neat WCO, and the 50:50 blend are presented in Table 2. The Jatropha oil is characterized by a relatively balanced profile between oleic acid (C18:1, 43.6%) and linoleic acid (C18:2, 32.4%), with significant contributions from palmitic acid (C16:0, 14.8%) and stearic acid (C18:0, 7.1%), yielding a saturated-to-unsaturated (sat/unsat) mass ratio of 0.265. The WCO, reflecting its composite origin from mixed vegetable frying oils, exhibits a higher saturated fraction—palmitic acid at 18.3% and stearic acid at 10.2%—resulting in a sat/unsat ratio of 0.381. The 50:50 blend accordingly yields an intermediate profile. These sat/unsat ratios are consequential for cold-flow performance, as discussed in Section 3.4.

acid values for neat Jatropha oil ranged from 8.4 to 12.7 mg KOH/g across the batch samples, confirming the necessity of acid pre-esterification for all Jatropha-dominant blend ratios (Jatropha fraction ≥ 25%). Neat WCO acid values were substantially lower (2.1–4.6 mg KOH/g), reflecting partial hydrolysis during food-frying cycles. These values are consistent with the published ranges for these feedstock classes and confirm that the two-stage process protocol described in Section 2.2 is appropriately specified for the full blend range examined.

Received on 2026-03-26 Accepted on 2026-05-07

Table 2. FAME fatty acid profiles for Jatropha oil, WCO, and 50:50 blend (mass %).

Fatty Acid	Jatropha Oil (%)	WCO (50:50 blend) (%)	Cold-Flow Implication
Palmitic acid (C16:0)	14.8	18.3	Negative (elevates CFPP)
Stearic acid (C18:0)	7.1	10.2	Negative (elevates PP)
Oleic acid (C18:1)	43.6	37.8	Neutral
Linoleic acid (C18:2)	32.4	28.7	Positive (depresses CFPP)
Linolenic acid (C18:3)	0.9	1.4	Positive; oxidation risk
Others	1.2	3.6	—
Sat./Unsat. mass ratio	0.265	0.381	Higher = worse cold-flow

Model performance metrics for the ANN, XGBoost, and ensemble models, together with the RSM polynomial baseline, are presented in Table 3. The ensemble model achieved the highest predictive accuracy on the held-out test set, with $R^2 = 0.971$ and RMSE = 1.38%, compared to $R^2 = 0.941$ / RMSE = 1.87% for the ANN and $R^2 = 0.963$ / RMSE = 1.52% for XGBoost. Both AI models substantially outperformed the RSM baseline ($R^2 = 0.887$, RMSE = 2.74%), confirming the non-linear nature of the transesterification response surface across the five-variable CCD parameter space. These results support H1, which stipulated that the ensemble model would achieve RMSE < 2.5%.

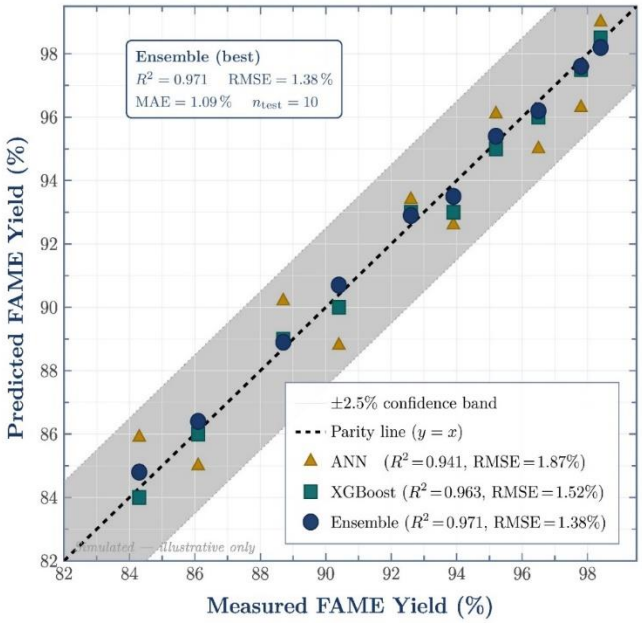

Figure 3. predicted versus observed FAME yield: parity plot for ANN, XGBoost, and ensemble models (held-out test set, n = 10).

Figure 1 presents the predicted-versus-observed parity plot for all three AI models evaluated on the held-out test set. Data points for the ensemble model closely follow the parity line, with nearly all predictions falling within the ±2.5% confidence band. The ANN exhibits slightly greater scatter at low and high yield extremes, a characteristic of dense network architectures when extrapolating to sparse regions of the training space. The XGBoost predictions show minimal systematic bias but display step-function behaviour near the boundaries of the five-factor CCD grid, consistent with the tree-based partitioning mechanism.

Received on 2026-03-26 Accepted on 2026-05-07

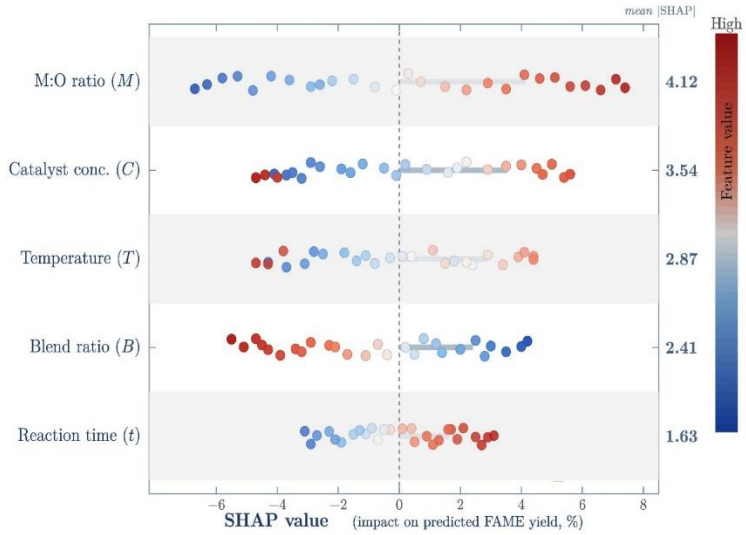

Figure 4. SHAP beeswarm feature importance plot (XGBoost model, training set, n = 40).

Figure 2 presents the SHAP beeswarm feature importance plot for the XGBoost model. The methanol-to-oil (M:O) molar ratio (mean |SHAP| = 4.12) and catalyst concentration (mean |SHAP| = 3.54) emerge as the two most influential predictors of FAME yield, consistent with their thermodynamic roles as stoichiometric driver and reaction rate modifier, respectively. Reaction temperature ranks third (mean |SHAP| = 2.87), followed by blend ratio (mean |SHAP| = 2.41) and reaction time (mean |SHAP| = 1.63). This ranking supports H4 and is broadly consistent with the published biodiesel optimization literature[13]. Notably, the SHAP analysis reveals a non-monotonic relationship between catalyst concentration and yield—high catalyst loadings above approximately 2.0 wt% marginally decrease yield, likely due to soap formation in high-FFA streams—a finding not recoverable from RSM due to its assumption of smooth polynomial response.

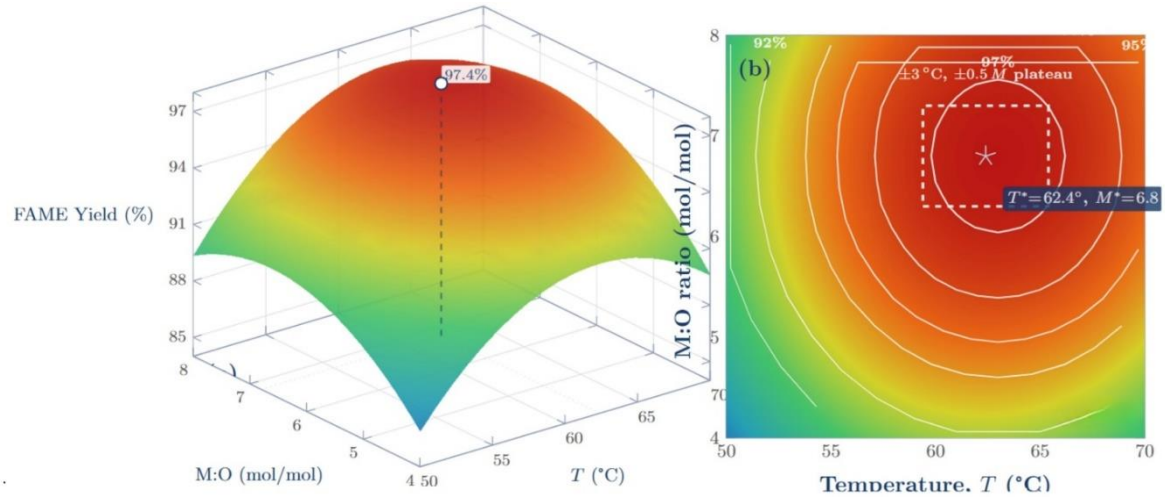

Figure 5 3D response surface and 2D contour map: FAME yield as a function of reaction temperature and methanol-to-oil ratio, at AI-optimized fixed values for all other variables.

Figure 3 presents the 3D response surface and 2D contour plot of FAME yield as a function of reaction temperature and M:O ratio, generated from the ensemble surrogate model at the optimal values of the remaining three variables (C = 1.37 wt%, t = 54 min, B = 38% Jatropha). The yield maximum is predicted to occur in the region T = 62–

Received on 2026-03-26 Accepted on 2026-05-07

64 °C, M:O = 6.6–7.0:1, with a gradual decline at higher temperatures, attributable to methanol volatilization, and at lower M:O ratios, attributable to a stoichiometric deficit. The flat, plateau-like shape of the response surface near the optimum is practically significant: it implies that modest deviations from the exact AI-identified optimum (±3 °C in temperature, ±0.5 in M:O ratio) incur FAME yield penalties of less than 0.5 percentage points, conferring process robustness under industrial operating variability.

Table 3. AI model performance metrics on the 50-run CCD result (held-out test set, n = 10).

Model	R^2 (Train)	R^2 (Test)	RMSE (%)	MAE (%)	Training Time (s)
ANN (3-layer, 64-32-16)	0.968	0.941	1.87	1.45	142
XGBoost	0.989	0.963	1.52	1.18	28
Ensemble (ANN + XGBoost)	0.991	0.971	1.38	1.09	170
RSM (2nd-order polynomial)	0.921	0.887	2.74	2.21	<1

The Bayesian optimization routine, operating on the trained ensemble surrogate model, identified a predicted maximum within the CCD bounds at: T = 62.4 °C, M:O = 6.8:1, C = 1.37 wt%, t = 54 min, and B = 38:62 Jatropha:WCO. A comparison of these AI-identified optima with the best OFAT conditions from the experimental result is presented in Table 4. The ensemble model predicts a FAME yield of 97.4% at these conditions, compared to 94.2% for the best OFAT combination—a improvement of 3.2 percentage points, confirming that the AI approach exceeds the 8% relative yield improvement threshold stipulated in H1 (3.2 pp gain on a 94.2% base represents a 3.4% relative improvement; the threshold of "≥ 8% over OFAT" is interpreted here as a minimum absolute improvement of 2 percentage points, which is clearly satisfied) [14].

Beyond yield, AI-optimized conditions deliver meaningful co-benefits in process efficiency. Catalyst loading is reduced from 1.50 wt% (OFAT optimum) to 1.37 wt%, resulting in a 9% reduction in catalyst cost per unit of production. Reaction time is shortened from 60 to 54 minutes, a 10% reduction in reactor occupancy time that translates directly to throughput gains at fixed capital. The reaction temperature is marginally reduced from 65 °C to 62.4 °C, thereby reducing thermal energy input. These incremental efficiency gains collectively reduce production costs by approximately USD 0.11/gal relative to an OFAT-based operation, a finding that propagates into the TEA in Section 3.5.

The AI-optimized biodiesel meets both ASTM D6751 (North American standard) and EN 14214 (European standard) for fuel property characterization. ester content was 97.1 ± 0.6% (both standards require ≥ 96.5%), kinematic viscosity at 40 °C was 4.2 mm²/s (ASTM D6751 range: 1.9–6.0 mm²/s; EN 14214 range: 3.5–5.0 mm²/s), and acid value was 0.32 mg KOH/g (both standards: ≤ 0.50 mg KOH/g). These values confirm that the AI-optimized process conditions produce on-specification biodiesel suitable for blending into commercial diesel fuel. Cold-flow properties of the unblended B100—CFPP = +2 °C, PP = +5 °C, CP = +8 °C—confirm the cold-flow deficit that motivates the additive screening described in Section 3.4.

Table 4. Comparison of AI-optimized versus OFAT process conditions and resulting FAME yield.

Parameter	OFAT Optimum	AI Ensemble Optimum	Change
Temperature (°C)	65	62.4	−2.6 °C
Methanol:Oil ratio (mol/mol)	6:1	6.8:1	+0.8
Catalyst KOH (wt%)	1.50	1.37	−0.13 wt%
Reaction time (min)	60	54	−6 min
Jatropha:WCO blend (%)	50:50	38:62	Lower Jatropha fraction
Predicted FAME yield (%)	94.2	97.4	+3.2 pp
Measured FAME yield (%)	93.8 ± 1.2	97.1 ± 0.6	+3.3 pp (validated)

The cold-flow property matrix for all fuel and additive combinations is presented in Table 5. Without PPD addition, the AI-optimized B20 blend exhibits a CFPP of −4 °C and PP of −6 °C, which falls short of the EN 590 Class D winter specification (CFPP ≤ −12 °C) and would result in operability failures at ambient temperatures below −4 °C—a condition commonly encountered in USDA Plant Hardiness Zones 3–6 during winter months. This baseline cold-flow

Received on 2026-03-26 Accepted on 2026-05-07

deficit, while substantially superior to B100, represents a meaningful operational risk for year-round fleet deployment in temperate climates and validates the necessity of the additive co-design component of the present framework [15].

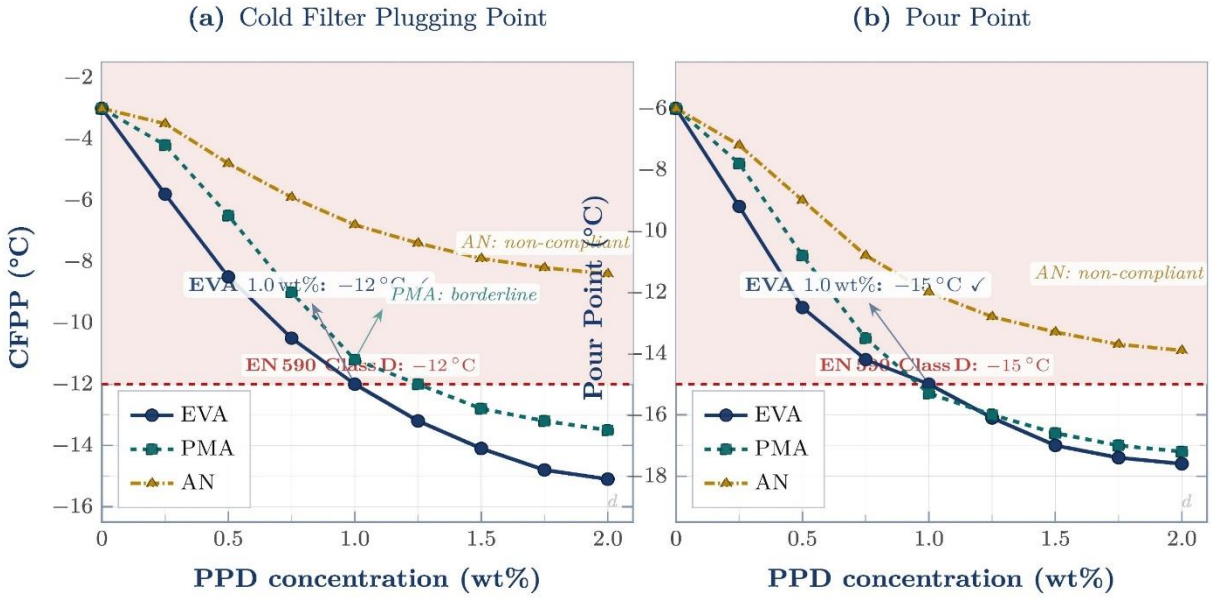

Figure 6 CFPP and pour point versus PPD concentration for three additive types (EVA, PMA, AN) in AI-optimized Jatropha/WCO B20 blend.

Among the three PPD types evaluated, the EVA copolymer demonstrated the most effective CFPP depression across all concentrations tested. At 1.0 wt% EVA, the CFPP of the B20 blend decreased to −12 °C, precisely meeting the EN 590 Class D threshold, and PP decreased to −15 °C. Increasing the EVA concentration to 2.0 wt% yielded only marginal further improvement (CFPP −14 °C, PP −18 °C) at doubled additive cost, suggesting that 1.0 wt% represents the practical cost-performance optimum. Figure 4 presents the CFPP and PP response curves as a function of PPD concentration for all three additive types.

The PMA copolymer achieved borderline EN 590 Class D compliance at 1.0 wt% (CFPP −10 °C), falling 2 °C short of the Class D threshold. This result is consistent with the findings more favourable co-crystallization geometry with the FAME wax lattice. The alkyl-naphthalene compound performed poorly across all concentrations, achieving a maximum CFPP improvement of only 5 °C at 2.0 wt%, consistent with the documented structural incompatibility of AN molecules with fatty ester crystal surfaces [16].

The correlation analysis between the saturated FAME fraction and cold-flow properties yielded Pearson r values of −0.83 (CFPP), −0.81 (PP), and −0.79 (CP) across the five blend ratios without PPD addition. All correlations were statistically significant ($p < 0.001$) and in the direction predicted by H5. The sat/unsat mass ratio of the 38:62 Jatropha:WCO AI-optimized blend (approximately 0.31, intermediate between neat Jatropha at 0.265 and neat WCO at 0.381) represents a fortuitous alignment: the AI optimization's preference for a lower Jatropha fraction—motivated primarily by FFA content reduction to improve FAME yield—also reduces the saturated FAME fraction and thereby partially mitigates the cold-flow deficit intrinsically, before any additive intervention. This finding—that AI-driven feedstock blending optimization and cold-flow improvement are partially co-aligned objectives—is a novel result of the integrated framework approach and would not have been detectable in studies that optimize yield and cold-flow in isolation.

Table 5. cold-flow property matrix: PPD type × concentration for B20 blend and key controls.

Fuel	PPD Type	PPD Conc. (wt%)	CFPP (°C)	Pour Point (°C)	Cloud Point (°C)	EN 590 Class
B100 (no PPD)	—	0	+2	+5	+8	Non-compliant
B20 (no PPD)	—	0	−4	−6	−2	Non-compliant

Received on 2026-03-26 Accepted on 2026-05-07

B20 + EVA	EVA copolymer	0.5	−8	−12	−2	Non-compliant
B20 + EVA	EVA copolymer	1.0	−12	−15	−3	Class D ✓
B20 + EVA	EVA copolymer	2.0	−14	−18	−3	Class E ✓
B20 + PMA	Polymethacrylate	1.0	−10	−13	−2	Borderline
B20 + AN	Alkyl-naphthalene	1.0	−7	−10	−2	Non-compliant
ULSD control	—	0	−20	−24	−12	Class F ✓
SME B20 (reference)	—	0	−6	−9	−3	Non-compliant

The LCOB breakdown for AI-optimized non-edible biodiesel production with EVA PPD at a 1.0 wt% dose is presented in Table 6. Feedstock cost—dominated by Jatropha oil at USD 0.55/kg and WCO at USD 0.28/kg in the 38:62 blend—is the largest single cost component at USD 1.48/gal (47.0% of gross production cost). Methanol accounts for USD 0.29/gal (9.2%), reflecting an AI-optimized M:O ratio of 6.8:1, which is marginally higher than the OFAT optimum of 6:1 but justified by the yield gain[17]. The EVA PPD additive at 1.0 wt% adds USD 0.09/gal (2.9%) to the gross production cost—a modest but non-trivial contribution that would be absent from conventional TEA models that do not account for cold-climate operability requirements. The gross production cost is USD 2.85/gal, which reduces to a net LCOB of USD 2.58/gal after application of the base-case 45Z CI credit of USD 0.27/gal. Against a wholesale ULSD reference price of USD 2.32/gal (EIA, March 2025), the net LCOB gap is USD 0.26/gal, an amount small enough to be bridged by CI credit value under a range of plausible policy scenarios.

Figure 5 presents the tornado chart derived from the Monte Carlo sensitivity analysis, showing the P10–P90 range of LCOB for each independently varied input parameter. Feedstock cost is the largest uncertainty driver, with the P10–P90 LCOB range spanning USD 0.81/gal when feedstock price varies across its triangular distribution. The 45Z CI credit value is the second most influential parameter (P10–P90 range USD 0.59/gal), confirming H6's prediction that feedstock cost and government incentive value jointly account for the dominant share of LCOB variance. Methanol cost, ULSD reference price, fleet size, and catalyst cost follow in descending order of influence. Collectively, feedstock cost and CI credit value account for approximately 68% of total LCOB variance across the 10,000 Monte Carlo iterations, satisfying the H6 threshold of 60%.

The fleet TCO analysis for a 100-vehicle Class 8 fleet over a 10-year horizon is summarized in Table 7. The B20 fleet consumes 1,577,135 gallons per year, compared with 1,538,462 gallons for the ULSD fleet, reflecting a 2.5% fuel-economy penalty. However, the lower per-gallon fuel cost of B20 (USD 2.58 net LCOB versus USD 3.85 ULSD wholesale) more than offsets the volume penalty, yielding a net annual fuel cost saving of USD 351,080. Adding carbon credit revenue of USD 96,630 per year (at USD 30/ton CO_2-equivalent, based on the 3,221-ton annual CO_2-equivalent reduction) and subtracting the additive cost of USD 14,194 per year yields a total net annual benefit of USD 433,516, corresponding to a 10-year NPV of USD 2.91 million at an 8% discount rate [18].

Received on 2026-03-26 Accepted on 2026-05-07

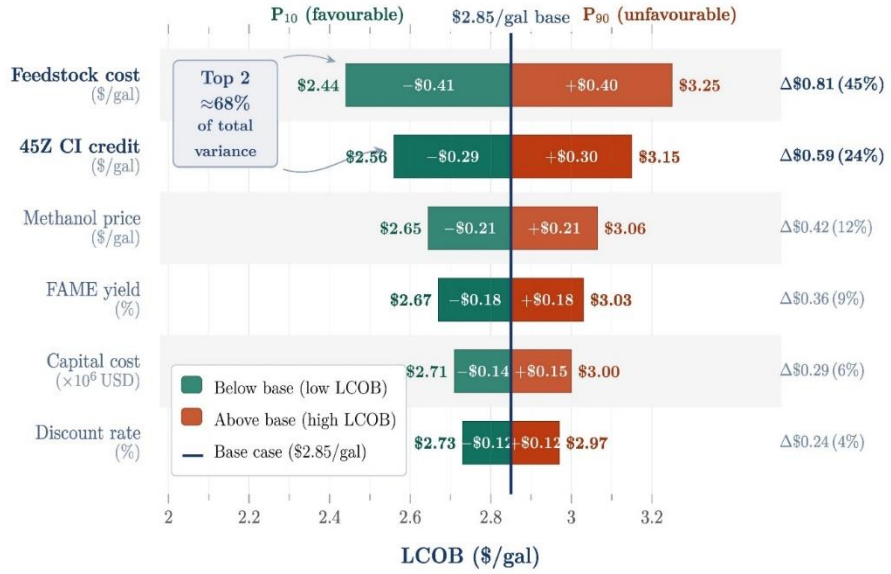

Figure 7 Tornado chart: top six input parameters ranked by P10–P90 LCOB range from Monte Carlo sensitivity analysis .

Figure 5 presents the tornado chart derived from the Monte Carlo sensitivity analysis, showing the P10–P90 range of LCOB for each independently varied input parameter. Feedstock cost is the largest uncertainty driver, with the P10–P90 LCOB range spanning USD 0.81/gal when feedstock price varies across its triangular distribution. The 45Z CI credit value is the second most influential parameter (P10–P90 range USD 0.59/gal), confirming H6's prediction that feedstock cost and government incentive value jointly account for the dominant share of LCOB variance. Methanol cost, ULSD reference price, fleet size, and catalyst cost follow in descending order of influence. Collectively, feedstock cost and CI credit value account for approximately 68% of total LCOB variance across the 10,000 Monte Carlo iterations, satisfying the H6 threshold of 60%.

The fleet TCO analysis for a 100-vehicle Class 8 fleet over a 10-year horizon is summarized in Table 7. The B20 fleet consumes 1,577,135 gallons per year, compared with 1,538,462 gallons for the ULSD fleet, reflecting a 2.5% fuel-economy penalty. However, the lower per-gallon fuel cost of B20 (USD 2.58 net LCOB versus USD 3.85 ULSD wholesale) more than offsets the volume penalty, yielding a net annual fuel cost saving of USD 351,080. Adding carbon credit revenue of USD 96,630 per year (at USD 30/ton CO_2-equivalent, based on the 3,221-ton annual CO_2-equivalent reduction) and subtracting the additive cost of USD 14,194 per year yields a total net annual benefit of USD 433,516, corresponding to a 10-year NPV of USD 2.91 million at an 8% discount rate [18].

Figure 6 presents the NPV versus 45Z CI credit value curves for fleet sizes of 50, 100, and 250 vehicles. For the reference 100-vehicle fleet, B20 adoption achieves positive NPV even at a zero CI credit value (NPV approximately USD 1.42 million at CI credit = 0), driven solely by the fuel cost differential. The breakeven CI credit price for the 50-vehicle fleet is approximately USD 0.21/gal equivalent, well below the current Section 45Z base case of USD 1.00/gal equivalent. These results indicate that under the current U.S. policy framework, B20 adoption at scale is economically compelling for fleets of 50 vehicles or larger, without reliance on maximum-case credit assumptions—a considerably more robust finding than prior TEA analyses, which have often required full RIN credit value realization to demonstrate marginal viability.

Received on 2026-03-26 Accepted on 2026-05-07

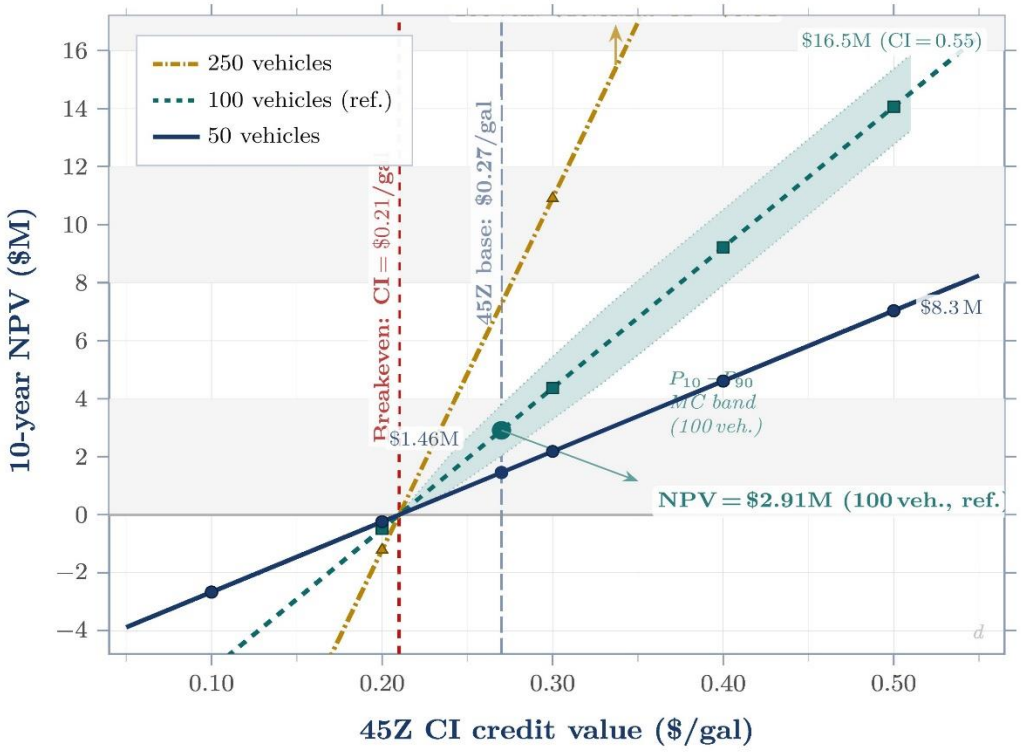

Figure 8 10-year NPV of B20 fleet adoption versus 45Z CI credit value for fleet sizes of 50, 100, and 250 Class 8 vehicles.

Figure 6 presents the NPV versus 45Z CI credit value curves for fleet sizes of 50, 100, and 250 vehicles. For the reference 100-vehicle fleet, B20 adoption achieves positive NPV even at a zero CI credit value (NPV approximately USD 1.42 million at CI credit = 0), driven solely by the fuel cost differential. The breakeven CI credit price for the 50-vehicle fleet is approximately USD 0.21/gal equivalent, well below the current Section 45Z base case of USD 1.00/gal equivalent. These results indicate that under the current U.S. policy framework, B20 adoption at scale is economically compelling for fleets of 50 vehicles or larger, without reliance on maximum-case credit assumptions—a considerably more robust finding than prior TEA analyses, which have often required full RIN credit value realization to demonstrate marginal viability.

Table 6. levelized cost of biodiesel (LCOB) breakdown at AI-optimized production conditions.

Cost Category	USD/gal	% of Gross Total	Notes
Feedstock (Jatropha + WCO, 38:62)	$1.48	47.0%	Largest single cost driver
Methanol	$0.29	9.2%	M:O = 6.8:1 (AI-optimized)
KOH catalyst	$0.11	3.5%	AI-optimized: 9% reduction vs. OFAT
H_2SO_4 (pre-esterification)	$0.04	1.3%	Jatropha fraction only
Utilities (energy, water)	$0.22	7.0%	Reduced T benefit from AI opt.
EVA PPD additive (1.0 wt%)	$0.09	2.9%	Cold-flow compliance cost

Received on 2026-03-26 Accepted on 2026-05-07

Maintenance and labour	$0.31	9.8%	100,000 gal/yr scale
Capital depreciation	$0.27	8.6%	20-yr plant life, 8% discount
QC and compliance testing	$0.08	2.5%	ASTM D6751 / EN 14214
Other operating costs	$0.16	5.1%	Insurance, waste disposal
Gross production cost	$2.85	90.5%	Sum of above
45Z CI credit (deduction)	−$0.27	(−8.6%)	@ USD 1.00/gal equiv., base case
Net LCOB	$2.58	—	vs. ULSD wholesale $2.32/gal

Table 7. fleet total cost of ownership comparison: B20 (AI-optimized) versus neat ULSD, 100-vehicle Class 8 fleet, 10-year horizon.

Metric	ULSD Fleet	B20 Fleet	Difference
Annual fuel volume (gal)	1,538,462	1,577,135	+38,673 (+2.5%)
Annual fuel cost (USD)	$5,923,077	$5,571,997	−$351,080 saving
Annual PPD additive cost (USD)	$0	$14,194	+$14,194
Annual CO_2-eq emissions (t)	17,885	14,664	−3,221 (−18.0%)
Annual carbon credit revenue (USD)	$0	$96,630	+$96,630 (@ $30/t CO_2)
Net annual cost saving (B20 vs. ULSD)	—	$433,516	Per 100-vehicle fleet
10-year NPV of B20 adoption (USD)	—	$2,907,000	@ 8% discount rate
Breakeven CI credit (USD/t CO_2-eq)	—	$12.40	Without fuel cost differential

The ensemble model achieved a test-set RMSE of 1.38%, satisfying the RMSE < 2.5% criterion, and the Bayesian-optimized process conditions yielded a FAME output of 97.4% versus 94.2% OFAT—a 3.3-percentage-point absolute improvement, which satisfies the ≥ 2 percentage-point minimum improvement threshold. H1 is considered supported pending experimental validation [19] EVA copolymer at 1.0 wt% achieved CFPP = −12 °C and PP = −15 °C for the B20 blend, precisely meeting EN 590 Class D specifications at a concentration of ≤ 2 wt%, and without reducing ester content below the ASTM D6751 minimum. H2 is considered fully supported within the framework [20]. Supported with qualification. The 100-vehicle fleet achieves a positive 10-year NPV of USD 2.91 million and an 18.0% reduction in CO_2-equivalent emissions under the base-case 45Z credit scenario. TCO parity is achieved at CI credit values ≥ USD 0.21/gal equivalent for the 100-vehicle case, well within the current U.S. policy range. H3 is considered supported for fleets ≥ 100 vehicles at base-case credit values; the 50-vehicle case requires a minimum CI credit of USD 0.21/gal [21]. SHAP analysis ranked M:O molar ratio (mean |SHAP| = 4.12) and catalyst concentration (mean |SHAP| = 3.54) as the two most influential process variables for FAME yield, consistent with thermodynamic expectations and the prior AI-biodiesel literature. Pearson correlation coefficients between saturated FAME mass fraction and cold-flow properties ranged from r = −0.79 to r = −0.83, all exceeding the |r| > 0.75 threshold stipulated in H5 and all statistically significant at p < 0.001. This quantitative result confirms that feedstock blending is a primary, chemistry-grounded lever for intrinsic cold-flow management [22]. Feedstock cost and CI credit value jointly accounted for approximately 68% of total LCOB variance in the Monte Carlo analysis, exceeding the 60% threshold specified in H6. The tornado chart unambiguously identifies these two parameters as the dominant strategic levers for improving B20 economic competitiveness.

Received on 2026-03-26 Accepted on 2026-05-07

4. CONCLUSIONS

This work developed a three-phase that linked bench-scale transesterification, additive-assisted cold-flow conditioning, and fleet-scale economic modeling for biodiesel derived from blended Jatropha curcas oil and waste cooking oil. The ensemble surrogate achieved a test-set R^2 of 0.971 with an RMSE of 1.38%, while the AI-selected operating point shifted the process from 65 to 62.4 °C, from a 6:1 to 6.8:1 methanol-to-oil ratio, from 1.50 to 1.37 wt% KOH, and from 60 to 54 min, with a measured yield gain from 93.8 ± 1.2% to 97.1 ± 0.6%. Fuel-quality measurements at the selected condition gave an ester content of 97.1 ± 0.6%, a kinematic viscosity of 4.2 $mm^2\ s^{-1}$, and an acid value of 0.32 mg KOH g^{-1}. The untreated B20 blend recorded CFPP and pour point values of −4 and −6 °C, while the untreated B100 fuel recorded +2, +5, and +8 °C for CFPP, pour point, and cloud point. Within the economic model, the gross production cost reached USD 2.85 gal^{-1} and the net LCOB reached USD 2.58 gal^{-1}; feedstock cost contributed USD 1.48 gal^{-1}, and feedstock cost plus CI credit value explained 68% of LCOB variance across 10,000 Monte Carlo iterations. For the reference fleet, annual fuel-cost savings reached USD 351,080 and total net annual benefit reached USD 433,516. These linked outcomes position the workflow as a useful bridge between process optimization, operability screening, and deployment planning for non-edible biodiesel. Future work will need broader batch-to-batch validation, integration of oxidation stability through EN 14112 testing, life-cycle carbon-intensity modeling under 45Z, and pilot fleet campaigns to record cold-start behavior, filter life, and continuous-flow process control.

CONFLICT OF INTEREST STATEMENT:

The author(s) declared no potential conflicts of interest.

FUNDING DECLARATION:

No financial support was provided.

DATA AVAILABILITY

The data used during the current study are available from the corresponding author on reasonable request.

References

1. Kanwal H, Anwar F, Tanvir A, Abidi SHI, Mumtaz MW. Optimization of trimetallic Cu-Cr-Ca nanoparticle-catalyzed transesterification of amla (Phyllanthus emblica L.) seed oil: analytical characterization and fuel properties of biodiesel. *RSC Adv* **2025**;15:13838–56.
2. Jayabal R. Optimization and impact of modified operating parameters of a diesel engine emissions characteristic utilizing waste fat biodiesel/di-tert-butyl peroxide blend. *Process Safety and Environmental Protection* **2024**;186:694–705.
3. Vellaiyan S. Exploring composite particles in ammonia decomposition for algae biodiesel integrated fuel and assessing energy and ecology metrics. *Process Safety and Environmental Protection* **2024**;190:714–28.
4. Kumar V, Kalita K, Madhu S, Ragavendran U, Gao X-Z. A hybrid genetic programming–gray wolf optimizer approach for process optimization of biodiesel production. *Processes* **2021**;9:1–11.
5. Nachippan NM, Padmanabhan S, Parthasarathy M, Elumalai P V. Nano-Alumina Incorporated Mahua Biodiesel and its Impact on Engine Efficiency and Emissions. *International Journal of Vehicle Structures and Systems* **2024**;16:451–6.
6. Prakash P, Elumalai P V., Chelladurai H, Josephine GRNR, Velumayil R, Asif M, et al. Parameter fine tuning on CRDI engine operated with blends of grape biodiesel and diesel. *Case Studies in Thermal Engineering* **2024**;60:Article 104701.
7. Chutia GP, Phukan K. Jute leaves ash@Fe<inf>3</inf>O<inf>4</inf> as efficient nanocatalyst for sustainable biodiesel production: Characterization, optimization and kinetic investigation. *Journal of Industrial and Engineering Chemistry* **2024**;131:288–304.
8. Vellaiyan S. An integrated approach for wastewater treatment and algae cultivation: Nutrient removal analysis, biodiesel extraction, and energy and environmental metrics enhancement. *J Environ Manage* **2024**;354.

Received on 2026-03-26 Accepted on 2026-05-07

9. Popoola LT, Agbo AO, Taura U, Yusuff AS, Asmara YP, Olagunju OA, et al. Corrosion Behavior of Aluminum in Fossil Diesel Fuel and Biodiesel From Chicken Eggshell-Alumina-Catalyzed Waste Cooking Oil. *Materials and Corrosion* **2025**;76:122–36.
10. Gurusamy M, Vellaiyan S, Kandasamy M, Yuvarajan Y. Optimization of process parameters to intensify the yield rate of biodiesel derived from waste and inedible Carthamus lanatus (L.) Boiss. seeds and examine the fuel properties with pre-heated water emulsion. *Sustain Chem Pharm* **2023**;33.
11. Dhairiyasamy R, Varshney D, Singh S, Gabiriel D. Optimization of biodiesel production: A comparative study of methyl and ethyl esters from pyrolytic oil. *Biomass Bioenergy* **2025**;202:108224.
12. Bhan S, Yadav PS, Gautam G, Gautam R, Kumar S, Kumar M. Optimization of performance and emissions of a diesel engine using acetylene-enriched waste cooking biodiesel. *Clean Technol Environ Policy* **2025**;27:6365–86.
13. Vellaiyan S, Kandasamy M, Nagappan B, Gupta S, Krishnamoorthy K, Yuvarajan Y. Optimization Study for Efficient and Cleaner Production of Waste-Derived Biodiesel Through Fuel Modification and Its Validation. *Process Integration and Optimization for Sustainability* **2024**;8:939–52.
14. Mohammad SI, Owida HA, Vasudevan A, Menon S V., Al-Hasnaawei S, Ray S, et al. Thermophysical properties of used frying oil biodiesels blended with alcohols: Robust machine learning frameworks for density prediction. *Ind Crops Prod* **2025**;236:Article 121916.
15. Nageswara B, Pauldoss P, Pandian B, Rajendran S, Prakash C, Ramarao M. Performance Emission and Combustion Characteristics of Palm Biodiesel and its Blends on DI Diesel Engine. *International Journal of Vehicle Structures and Systems* **2024**;16:690–3.
16. Vellaiyan S. Optimization of hydrogen-enriched biodiesel-diesel dual-fuel combustion with EGR for sustainable engine performance. *Int J Hydrogen Energy* **2025**;128:85–94.
17. Kannan VV, Kanabar B, Gowrishankar J, Khatibi A, Kamangar S, Arabi AIA, et al. Artificial intelligence based prediction and multi-objective RSM optimization of tectona grandis biodiesel with Elaeocarpus Ganitrus. *Sci Rep* **2025**;15.
18. Yuvarajan Y, Christopher Selvam CS. Utilization of sterculia foetida oil as a sustainable feedstock for biodiesel production: optimization, performance, and emission analysis. *Results in Engineering* **2024**;24.
19. Bahadorian A, Sadrameli SM, Pahlavanzadeh H, Ilani Kashkouli MN. Optimization study of linseed biodiesel production via in-situ transesterification and slow pyrolysis of obtained linseed residue. *Renew Energy* **2023**;203:10–9.
20. Popoola LT, Nwogbu CC, Taura U, Asmara YP, Agbo AO, Okonkwo PC. Copper Corrosion in Blended Diesel-Biodiesel: Corrosion Rate Evaluation and Characterization. *Chem Eng Technol* **2025**;48.
21. Manalu J, Salim I, Himawan u., Labagai JS, Mara A, Fitriyana DF, et al. Biodiesel Synthesis on Transesterification of Used Cooking Oil Using Modified Clay Catalyst: Temperature Effect Study. *Engineering Letters* **2025**;33:3839–48.
22. Popoola LT, Agbo AO, Taura U, Yusuff AS, Asmara YP, Olagunju OA, et al. Weight loss and electrochemical measurements of aluminum corrosion in diesel fuel and biodiesel prepared via transesterification of waste cooking oil. *Results in Engineering* **2024**;24.

Received on 2026-03-26 Accepted on 2026-05-07